WILEY-VCH

In-Sensor Computing with Visual-Tactile Perception Enabled by Mechano-Optical Artificial Synapse

Jiaxing Guo†, *Feng Guo*†, *Huijun Zhao*†, *Hang Yang, Xiaona Du, Fei Fan, Weiwei Liu, Yang Zhang,* * *Dong Tu* *& *Jianhua Hao* *

J. Guo, H. Zhao, F. Fan, W. Liu, Y. Zhang

Institute of Modern Optics and Tianjin Key Laboratory of Micro-Scale Optical Information Science and Technology, Nankai University, Tianjin 300071, P. R. China

F. Guo, J. Hao

Department of Applied Physics, The Hong Kong Polytechnic University, Hung Hom, Hong Kong, P. R. China

H. Yang, D. Tu

Faculty of Materials Science and Chemistry, China University of Geosciences, 388 Lumo Road, Wuhan 430074, P. R. China

X. Du

Institute of Photoelectric Thin Film Devices and Technology, College of Electronic Information and Optical Engineering, Nankai University, Tianjin 300071, China

D. Tu

Wuhan University Shenzhen Research Institute, Shenzhen, 518057, China

E-mail: *yangzhang@nankai.edu.cn ,*tudong@cug.edu.cn and*jh.hao@polyu.edu.hk

†These authors contributed equally to this work.

Keywords: In-sensor computing, visual-tactile perception, mechano-optical artificial synapse, mechanoluminescence, photostimulated luminescence

Abstract: In-sensor computing paradigm holds the promise of realizing rapid and low-power signal processing. Constructing crossmodal in-sensor computing systems to emulate human sensory and recognition capabilities has been a persistent pursuit for developing humanoid robotics. Here, we report an artificial mechano-optical synapse to implement in-sensor dynamic computing with visual-tactile perception. By employing mechanoluminescence (ML) material, we achieve direct conversion of the mechanical signals into light emission and transport the light to an adjacent photostimulated luminescence (PSL) layer without pre- and post-irradiation. The PSL layer acts as a photon reservoir as well as processing unit for achieving in-memory

computing. The approach based on ML coupled with PSL material is different from traditional circuit–constrained methods, enabling remote operation and easy accessibility. Individual and synergistic plasticity are elaborately investigated under force and light pulses, including paired pulse facilitation, learning behavior, short-term and long-term memory. A multisensory neural network is built for processing the obtained handwritten patterns with a tablet consisting of our device, achieving a recognition accuracy of up to 92.5%. Moreover, material identification has been explored based on visual-tactile sensing, with an accuracy rate of 98.6%. Our work provides a promising strategy to construct in-sensor computing systems with crossmodal integration and recognition.

1. Introduction

Current sensing and processing systems consisting of separated sensing and computing units have led to unfavorable signal latency and energy consumption due to redundant data transmission.[1-6] Therefore, its performance falls far short of expectation to meet the demands of artificial intelligence applications. Moreover, electromagnetic interference is also a problem for processing and computing by electrical signal when facing high-throughput information. The biological nervous system, with the features of in-memory sensing and computing, provides important inspiration for designing its artificial counterpart.[7,8] The exceptional fault tolerance and power-efficient manners enable the biological system to compactly and effectively tackle complex real-world problems, and response to them in a dynamic manner.[9-17] Thus, emulating the functions of human sensing system can pave a critical way for advancing the performance of current hardware.[18-23] To date, neuromorphic behaviors which mimic the functions of single synapse have been widely investigated, and various perceptive abilities have also been integrated in the device.[24-28] Compared to the single-type perception, multimodal sensing capacity can provide more comprehensive information,[29-33] thereby effectively improving the accuracy of back-end neural networks in decision-making. Among the five perceptions including vision, hearing, smell, taste and touch, the combination of vision and touch is very important for industrial applications. For example, robots rely on the visual information to determine the position of the object, and rely on tactile information to know whether the object has been gripped.[34-37] However, achieving multimodal perception in a neuromorphic device is still a huge challenge due to the limited option for functional materials and device architectures.[38,39]

Mechanoluminescence (ML) allows quantitative conversion of mechanical stimuli into light emission in an in-situ and real-time manner.[40-42] Such force-to-light conversion enables the

construction of the visual-tactile perception sensor without the need of electrical or optical power supply.[43] Nevertheless, the current available ML materials intrinsically emit instantaneous luminescence under mechanical stimuli, which are not capable of storing information and performing neuromorphic computing. Thus, combining ML materials with optical storage functional materials is a good way to solve this problem. Photostimulated luminescence (PSL) phosphors can capture photons into traps and release them as light emission upon near-infrared (NIR) irradiation.[44,45] Once there is a substantial overlap between the ML emission spectra and the absorption spectra of PSL, the traps are ideal to construct an in-sensor optical memory. Furthermore, the trapping and detrapping process endow the system with the possibility for applications as a computing unit in future.

In this work, we construct a mechano-optical artificial synapse that combines ML material with PSL phosphor to enable in-sensor computing. The mechanical force and visible light work as input signals for emulating stimuli to pre-synapse, and the PSL signal serves as post-synapse response. The sensitive skin receptor based on 3D-printing layer and ML layer converts the mechanical signals into light emission and transport it to adjacent PSL layer. Then, the PSL layer acts as a photon reservoir as well as processing unit owing to the photon capture capability and electrons detrapping process upon NIR irradiation. The architecture of the device circumvents the incorporation of circuitry, and facilitates remote operation and accessibility, which is beneficial to wide practical applications. Besides, the device demonstrates neuromorphic features including short-term plasticity, long-term plasticity, paired-pulse facilitation, and "learning experience" in response to visual and tactile stimuli. Moreover, the cooperation of visual and tactile perception is demonstrated in our device, and the high recognition accuracy of artificial neural networks by multimodal sensing shows the great potential for processing complex information in a sophisticated way.

2. Results and Discussion

2.1. Device architecture and principles

The human brain demonstrates remarkable capability in learning and adapting to the complex real world through integrating different perceptions including vision, touch, hearing, smell and taste. Among the captured external information, 80% is visual information, which is obtained by the retina and subsequently transmitted to the brain for processing. On the other hand, the tactile sense offers intimate details about the hardness, force, vibration, and other tactile properties of objects encountered. The combination of them is highly desired for the realization of robots. In the biological nervous system, analysis of visual and tactile perception enables rapid and appropriate response to the external environment, as shown in **Figure 1**a.

Drawing inspiration from the biological multimodal perception mechanism, an artificial tactile-visual multimodal synapse is proposed, which integrates information perception capabilities with neuromorphic functions, as depicted in Figure 1b. The artificial synapse is made up of three layers, with the top two layers serving as the primary functional materials. The first layer comprises the PSL phosphor with photon capture ability, while the subsequent layer is composed of ML material for emitting light driven by mechanical force. The bottom layer, designated as the mechanical microstructure layer, is used to enhance the mechanical sensitivity of the device. The PSL layer is used as a visual perception sensor and artificial synapse. The ML layer and the 3D-print mechanical microstructure layer convert mechanical signals into optical signals for modulating the plasticity of synapse. The preparation process is illustrated in **Figure S1** of Supporting Information (details in "Methods" section). ZnS:Cu serves as the functional material in the ML layer, while $Ca_{0.25}Sr_{0.75}S$:Eu (CaSrS:Eu) is utilized as the PSL material. Additionally, **Figure S2** of Supporting Information showcases the scanning electron microscopy (SEM) images of ZnS:Cu and CaSrS:Eu particles. **Figure S3** shows the X-ray diffraction (XRD) patterns of ZnS:Cu and CaSrS:Eu powders, respectively. By comparing with the standard PDF cards, it is confirmed that they are single-phase materials with the dopants homogeneously distributed within the host matrices. Moreover, energy-dispersive spectroscopy (EDS) analysis (**Figure S4** and **S5** in the Supporting Information) and X-ray photoelectron spectroscopy (XPS) analysis (**Figure S6** and **S7** in the Supporting Information) were carried out on the materials. These results are consistent with the chemical compositions of ZnS:Cu and CaSrS:Eu, from which it can be inferred that all the elements are homogeneously incorporated into the materials. The optical microscope images of the ML and PSL layers reveal a uniform distribution of CaSrS:Eu and ZnS:Cu phosphors within the matrix. As shown in **Figure S8**, these two layers exhibit close adhesion and a uniform thickness.

ZnS:Cu materials exhibit remarkable ML emission when subjected to strain, and pre- and post-irradiation is not required. When the ZnS:Cu/PDMS composite is subjected to mechanical force, the triboelectric effect generates a quantity of charge that accumulates at the interface between the ZnS:Cu particle and the PDMS matrix. The resulting electric field exceeds the threshold value of the electric field (10^5 V/cm) necessary to trigger the electroluminescence of ZnS:Cu.[43] Consequently, the observed green emission, stemming from the $4T^1$–$6A^1$ transition of the Cu^{2+} ion, can be attributed to triboelectricity-induced luminescence.[46] Compared with other prevalent ML materials, ZnS:Cu, due to its superior properties, is rendered an indispensable ML material in device design (**Figure S9** of Supporting Information). Rare earth (RE)-doped CaSrS is regarded as promising PSL phosphor owing to the substantial overlap between the ML

emission spectra of ZnS:Cu and the absorption spectra of CaSrS:Eu, as depicted in **Figure S10** of Supporting Information. This overlap indicates the possibility of an energy transfer process occurring within this composite system. Moreover, the distribution of traps within CaSrS:Eu enables capturing electrons into traps. And the release of electrons occurs upon exposure to NIR irradiation or heating, which plays the role of tactile perception. Besides, the absorption spectrum of CaSrS:Eu encompasses a broad range below 650 nm, and it substantially overlaps with the primary wavelength spectrum of visible light (380-760 nm), covering most of the range of human vision. Under appropriate light stimuli, the electrons of Eu^{2+} located at the octahedral site (O_h) of the CaSrS lattice are pumped from the ground $4f^7$ state to the upper $4f^65d^1$ state, which overlaps with the conduction band.[47,48] Subsequently, the electron traps positioned beneath the conduction band minimum of CaSrS effectively capture partial electrons in the conduction band.[49,50] When irradiated by NIR light, the electrons within the traps are gradually excited, triggering continuous red PSL. The band structures of the ML layer and the PSL layer, as well as the operating mechanism of the device are shown in **Figure S11** and **Figure S12**of Supporting Information. The PSL spectrum and the 980 nm light source spectrum are displayed in **Figure S13**. Inspired by these intriguing characteristics, a concept of in-sensor computing and multimodal perception for AI applications is proposed.

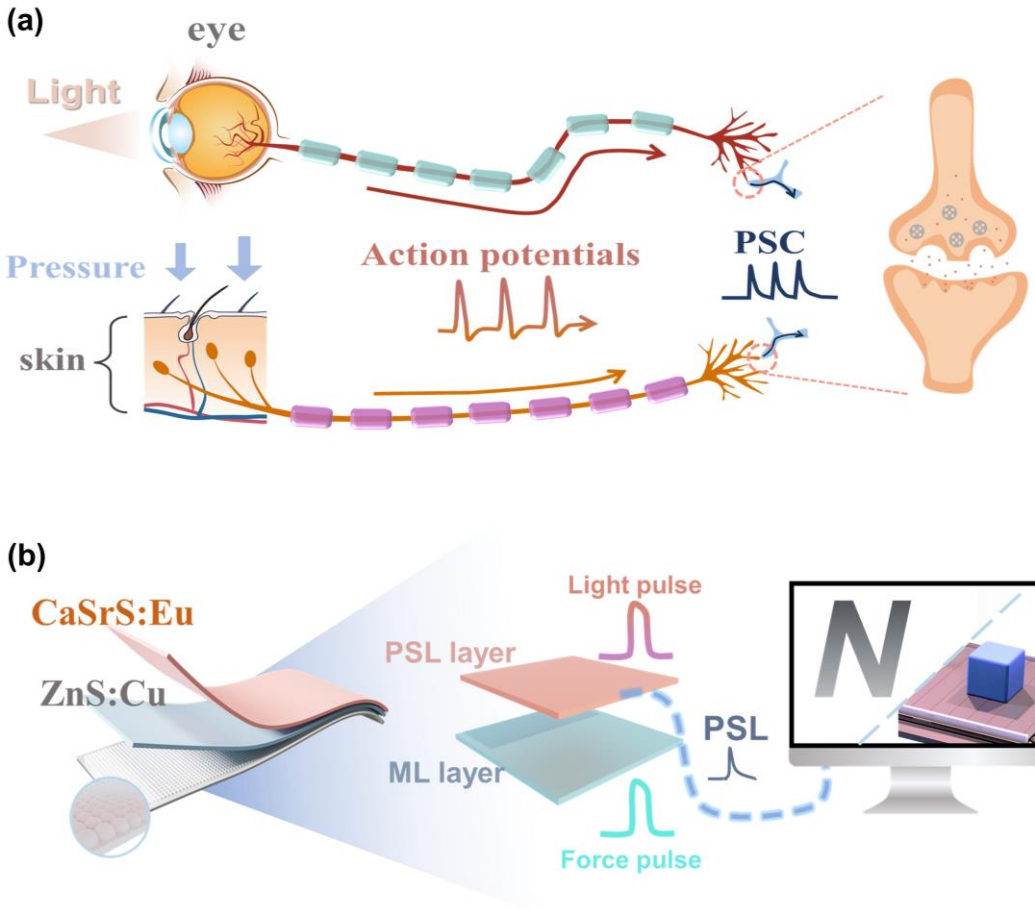

Figure 1. Artificial visual-tactile perception system for in-sensor computing inspirated by biological synapses. a) Schematic of human eye and skin that is capable of visual and tactile perception. b) Schematic illustrations of artificial visual-tactile synapse for in-sensor computing enabled by the consisting of photo-stimulated luminescence (PSL) material and mechanoluminescent (ML) layer. The sensitive skin receptor based on 3D printing layer and ML layer converts the mechanical signals into light emission and transport light to adjacent PSL layer. Then, PSL layer acts as photon reservoir as well as processing unit owing to the photon capture capability and detrapping process upon NIR irradiation.

2.2. Device performance characterization

To verify the device's capacity to mimic visual perception, a series of light pulses was applied to the device. As depicted in Figure 2a, the frequency of light pulse (λ=460 nm, 2.5 mW cm^{-2}) is 1 Hz and the pulse width is 0.5 s. The PSL signal read out by 980 nm light with 1.67 W cm^{-2} exhibits a pronounced increase under excitation by 460 nm light pulses. However, once the charging process induced by 460 nm light pulses is completed, there is no additional increase in the total number of electrons trapped in the traps. As a result, a low-power 980 nm light source has a lower pumping rate, enabling the gradual release of trapped electrons and a corresponding gradual decrease in the PSL signal. In contrast, a high-power 980 nm source has a higher pumping rate, allowing it to deplete all the electrons trapped in the traps in a shorter time, leading to a rapid decay of the PSL signal. The process plays the role of erasing memory-related information. To avoid interference, PSL signals are not recorded during the erasure operation. Therefore, when the 460 nm light pulse is removed, the PSL intensity gradually decreases. Notably, the utilization of a high-powered 980 nm (3.33 W cm^{-2}) source effectively eliminates this segment of the PSL signal, demonstrating the device's potential in optical writing and erasure. Furthermore, the 500 operational cycles exhibit remarkable stability of the device, as depicted in **Figure S14** of Supporting Information. The PSL intensity after imposing the 460 nm light pulse is determined as the transient intensity, serving as a metric to quantify the device's immediate response to the light pulses. **Figure S15** of Supporting Information illustrates the trend of these transient intensities under varying durations and light pulse powers under 1 Hz. When the 460 nm light pulse number is fixed at 20, a clear relationship between the transient intensity and the power of the light pulses can be observed, as depicted in Figure 2b. Subsequently, we further explored the impact of wavelength on the response of the PSL layer. The spectra of three light sources employed in the testing are presented in **Figure S16** of Supporting Information, while Figure 2c illustrates markedly distinct responses exhibited by our synaptic device under different wavelengths, at an identical power density of 2.5 mW cm^{-}

[2]. It indicates that the device can perceive and record different optical information, including wavelength and intensity. Intriguingly, the power of the 980 nm light source demonstrates the ability to modulate the photonic response of the device. As the power density of 980 nm light source increases, more trapped electrons are excited into the conduction band of CaSrS:Eu. These electrons then transition back to the ground state, resulting in an enhanced PSL. This mechanism is analogous to that of the adaptability of human iris, which adjusts its pupil size to accommodate varying light conditions and regulate the amount of light perceived. By precisely manipulating the power of the NIR source, it is feasible to modulate the PSL intensity to a nearly uniform level (as depicted by the gray area in Figure 2d) across different wavelengths, confirming remarkable flexibility and tunability.

Taking advantage of the photonic non-volatility, the device is utilized to mimic the neuromorphic functions in the human brain. Short-term plasticity (STP), long-term plasticity (LTP), and the transition between them are demonstrated for brain learning and decision-making processes. LTP serves as the cornerstone for memory by experiencing repeated events. Intense events and powerful stimuli are beneficial for promoting the formation of long-term memory (LTM). The transition from short-term memory (STM) to LTM was successfully emulated by adjusting the number of light pulses (Figure 2e), pulse interval (Figure 2f), and pulse width (**Figure S17** of Supporting Information). For example, as the number of 460 nm light pulses increases, there is a marked rise in the PSL intensity. In the experiments, to thoroughly exhibit the non-volatile optical states of the device's PSL response, we made use of the first few tens of light pulses. After light pulses are imposed on the device, the intensity will take more time to decay back to its initial state due to the increased number of light pulses (**Figure S18** of Supporting Information). It is also considered as a transition from STM to LTM. The light pulses with different interval time applied to the device are plotted in detail (**Figure S19** of Supporting Information). STP occupies a pivotal position in the efficient processing and decoding of temporal information in the nervous system, which mainly includes paired pulse facilitation (PPF) and post-tetanic potentiation (PTP). Specifically, if the number of electrons in the traps does not return to the initial level before the arrival of subsequent pulses, a cumulative effect arises after the termination of the initial pulse. This cumulative effect increases the PSL signal intensity. Therefore, the interval time between pulses plays a crucial role in regulating the amplitude of PSL. To emulate STP, the pulse interval (frequency) applied to the device is adjusted with a consistent pulse width of 0.5 s. Figure 2g and **Figure S20** of Supporting Information depict the trend of PPF and PTP, respectively. The trends show that as

the interval time of light pulses increases, the behavior is similar to that of biological systems.[51,52] In addition, the device also performs well in mimicking human "learning experience". Learning behavior consists of three core processes: learning, forgetting, and relearning. As external stimuli (460 nm light pulse) are repeated, the number of electrons stored in the material gradually accumulates, resulting in a marked rise in the PSL intensity read out by the 980 nm light (1.67 W cm^{-2}). The process exhibits behavior similar to that of memory retention in humans. After the removal of the external stimulus (460 nm light pulse), the electrons stop to accumulate. Under the irradiation of 980 nm light with a power density of 1.67 W cm^{-2}, the electrons in the CaSrS:Eu layer are gradually released. This leads to a decrease in the PSL signal of the device. This process can be employed to simulate the phenomenon of human forgetting. If the external stimulus is reapplied prior to the complete depletion of electrons, the electrons will resume their accumulation. This enables the number of electrons stored in the device to reach previous levels in a shorter period of time, Therefore, the re-learning time is shorter than that of the initial learning. As depicted in Figure 2h, after 15 light pulses and a forgetting period, merely 5 pulses are required to quickly restore the amplitude of the PSL signal. Following the removal of light pulses, the decay process of PSL can be well fitted to the memory-loss curve (**Figure S21** of Supporting Information), and the typical time constant is 0.34 s, which is in the range of human sensory memory (0.2~3 s). Moreover, to validate the stability of the device's performance in ambient conditions, it was subjected to a seven-day storage period at a fixed temperature of 26 ℃. The device's light responses were tested on the first, third, and seventh day of this period. As evidenced in **Figure S22** of Supporting Information, no notable variation was observed during these tests, demonstrating the system's exceptional operational reliability and stability under ambient conditions.

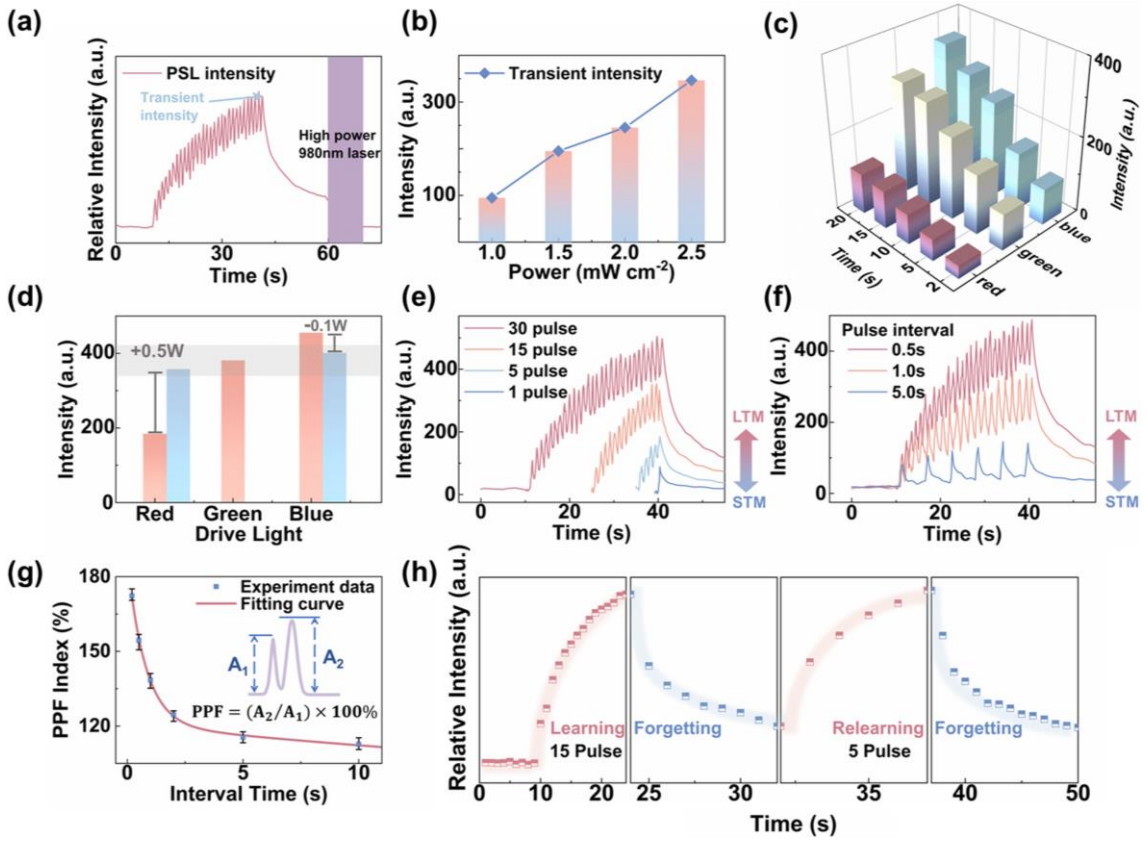

Figure 2. Photonic responses and visual in-sensor perception of the synaptic device. a) Characteristic photonic response of the device under 460 nm light pulses and high power 980 nm light erasing (purple regions). PSL intensity is read out by the 980 nm light (1.67 W cm^{-2}). PSL layer of the device acts as photon reservoir as well as processing unit to enable in-sensor computing. b) Light power-modulated photonic response. The transient intensity was recorded immediately after the light was turned off. c) The device's responses variation with various time and wavelength (the light pulses intensity is 2.5 mW cm^{-2}). d) By tuning the power of 980 nm source, the response under varying light wavelength modulated to same level (grey bars). This mimics the adaptive optical perception under different illumination conditions of the human eye. The transformation from STM to LTM achieved by varying the number e) of the light pulse and the frequency f) of light pulse (wavelength =460 nm, power density =2.5 mW cm^{-2}, width =500 ms). g) PPF index variation with the interval time between light pulses. The error bars represent the fluctuation from three measurements. h) The learning-experience behavior of the device under light pulses.

The ML layer transfers tactile stimuli to photon emission, which can be absorbed by the adjacent PSL layer. Subsequently, synaptic plasticity is dynamically modulated by a continuous 980 nm light source for the realization of tactile perception. To enhance the mechanical sensitivity of the device, the ML layer was strategically positioned on a mechanical microstructure layer crafted via precise 3D-printing techniques. We utilized the finite element analysis (COMSOL) to simulate the ML response of the device under external force, the results are shown in **Figure S23** of Supporting Information. Beyond the threshold of 2.5 kPa force, the ML intensity exhibits an upward trend, with the magnitude of the applied external force (**Figure 3**a). To gain a deeper understanding of the mechanical responsiveness of our synaptic device,

mechanical pulses were imposed at a fixed frequency of 1 Hz. Figure 3b illustrates the trend of the device's response over time under different amplitudes of force pulse. **Figure S24** of Supporting Information reveals that the transient intensity of the device changes with the amplitude of the following 20 force pulses. Interestingly, two ML response peaks are obtained by the application of a single force pulse. The phenomenon can be attributed to the twice friction between ZnS:Cu particles and the matrix material (PDMS) during the compression and subsequent decompression induced by a single force pulse. Similar phenomena have been reported in the previous literature.[46] The results exhibit a clear distinction between mechanical perception and visual perception (Figure 3c), providing the potential to process visual and tactile perception signals independently. In addition, the force response of the device (PSL intensity) can also be modulated by setting the appropriate 980 nm light source power (**Figure S25** of Supporting Information). This modulation is similar to how tactile nerves in different parts of the human body, respond with different degrees of sensitivity to external forces.

Subsequently, an exploration was conducted into the mechanical properties of the synaptic device. Analogous to visual perception, LTP and STP were emulated through the response of the device to force pulses with different numbers and frequencies. As depicted in **Figure S26** of Supporting Information, the increase in the number of force pulses (12.5 kPa, 1 Hz) elicited higher response from the device, showing a transition from STM to LTM manifested by an extended decay period subsequent to the remove of force pulses (**Figure S27** of Supporting Information). Furthermore, this effect could be achieved by modulating the time interval (or frequency) between successive force pulses, as illustrated in **Figure S28** of Supporting Information. The specific waveform of the ML pulses employed in this process is provided in **Figure S29** of Supporting Information. The PPF (Figure 3d) and PTP (**Figure S30** of Supporting Information) have been effectively replicated through two and ten consecutive mechanical pulses, demonstrating the short-term plasticity. Figure 3e illustrates the device's force-modulated "learn-forget-learn" cycle, where merely six force pulses are sufficient to restore the PSL amplitude after an exposure of 15 pulses and a forgetting period. Furthermore, the device's flexibility is demonstrated by its notable bending capabilities. **Figure S31** of Supporting Information shows the reliability after repeated bending, thus it is highly promising for future flexible photonic applications. After seven days' storage in ambient conditions, the force response exhibited few variations (**Figure S32** of Supporting Information), which confirms the environmental stability of the device.

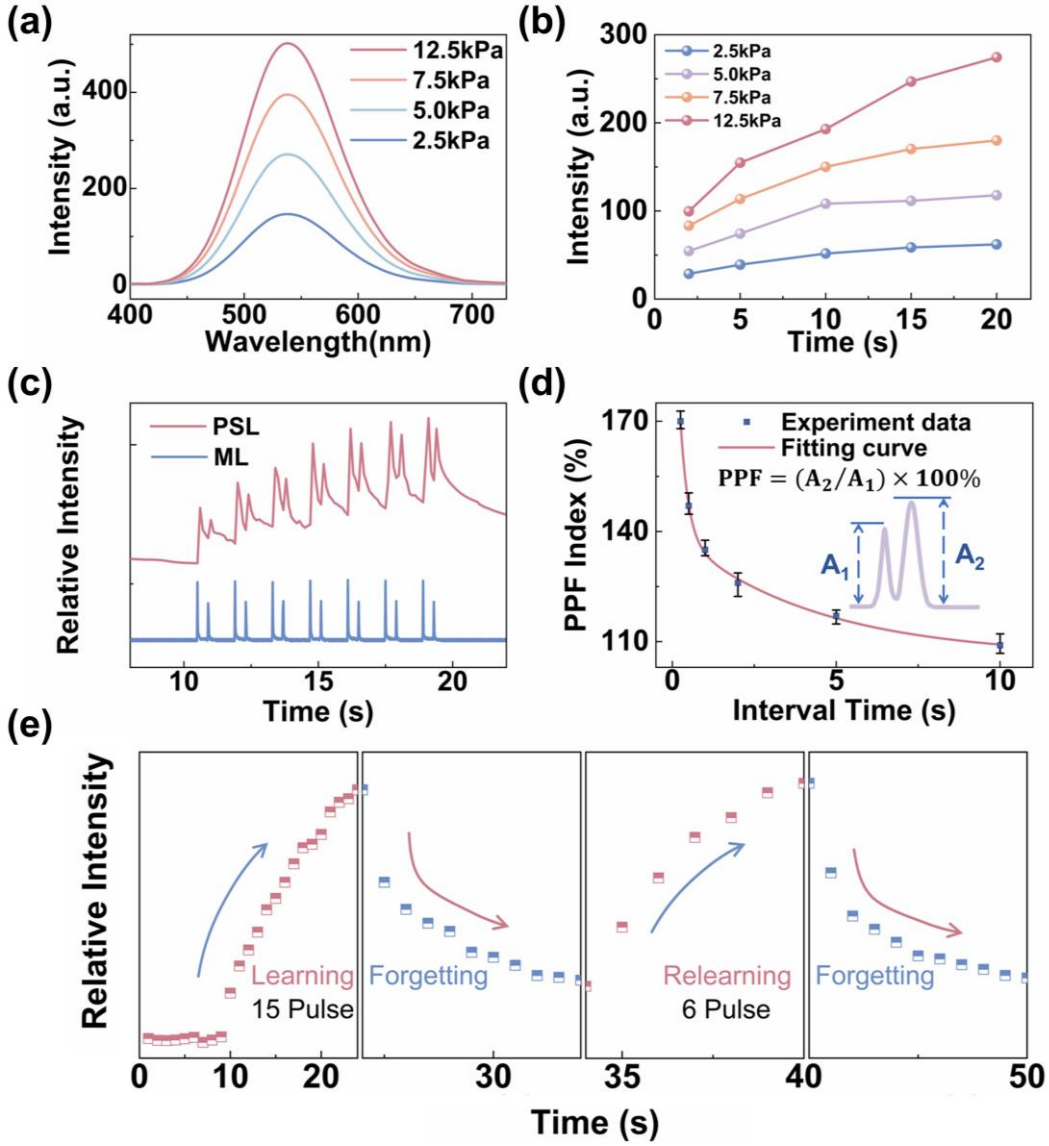

Figure 3. Mechanical responses and tactile perception of the synaptic devices. a) The response of the ZnS:Cu layer variation with different force magnitudes. b) The device's responses variation with various time and force (the mechanical pulses frequency is 1 Hz). The ML layer converts the mechanical signal into emitted light and transmits the light to the adjacent PSL layer for plasticity. The PSL signal is readout through 980 nm light (1.67 W cm^{-2}). c) The device's response and corresponding ML waveform. A single force pulse will trigger twice ML phenomenon, and the device's response also exhibits two spikes. d) PPF index variation with the interval time between mechanical pulses. The error bars represent the fluctuation from three measurements. e) The learning-experience behavior of the device under mechanical pulses.

2.3. Device applications

An array device was fabricated for verifying the ability of the device to capture and process images by visual and tactile senses. The pattern of light excitation is initially prepared by a front-end mask and then projected onto the surface of the PSL layer. Simultaneously, a patterned mechanical excitation is applied to the bottom of the ML layer, which subsequently conveys this information to the PSL through the mechanical-photo conversion properties of the ML

material, as illustrated in **Figure 4**a. **Figure S33** of Supporting Information presents the image of the array device. The result of the array device's response to a series of 30 sequential mechanical pulses (12.5 kPa, interval time 1 s) and light pulses (2.5 mW cm^{-2}, pulse width 0.5 s, interval time 1 s, and λ = 460 nm) is presented in Figure 4b. Supplementary video 1 demonstrates different excitation and the corresponding variation process of the patterned PSL signal from the device under these conditions. For clarity, the response spectrum under the first seven pulses is showcased in Figure 4c. This illustration demonstrates that the synchronized optical-mechanical pulse signal leads to a more pronounced response from the device than either optical or mechanical pulses along. An artificial neural network (ANN) was built and trained under supervised learning. The optical states are extracted from the device and mapped as synaptic weights of the ANN. The images obtained by the visual-tactile perception array are collected to create three databases including visual, tactile, and visual-tactile information respectively, as depicted in Figure 4d. This neural network comprises an input layer with 784 neurons, the hidden layer and output layer are composed of 50 and 5 neurons respectively. The image is divided into 28×28 pixels, transformed from PSL intensity. The brightness of these pixels are multiplied by a predefined weight matrix and activated by the sigmoid activation function to yield an output vector. The difference between output and target value is used for updating the weights of synapses in the neural network (backpropagation algorithm), as show in **Figure S34** of Supporting Information. The patterns created by the cooperation of force and light are clearer than those of only force or light mode. This improvement is attributed to the increased response intensity of the device when subjected to simultaneous force and light pulses. As depicted in Figure 4e, the recognition accuracy of visual-tactile perception increases significantly with the number of training epochs and reaches up to 92.5%, which is higher than that of tactile perception (69.6%) or visual perception (79.6%).

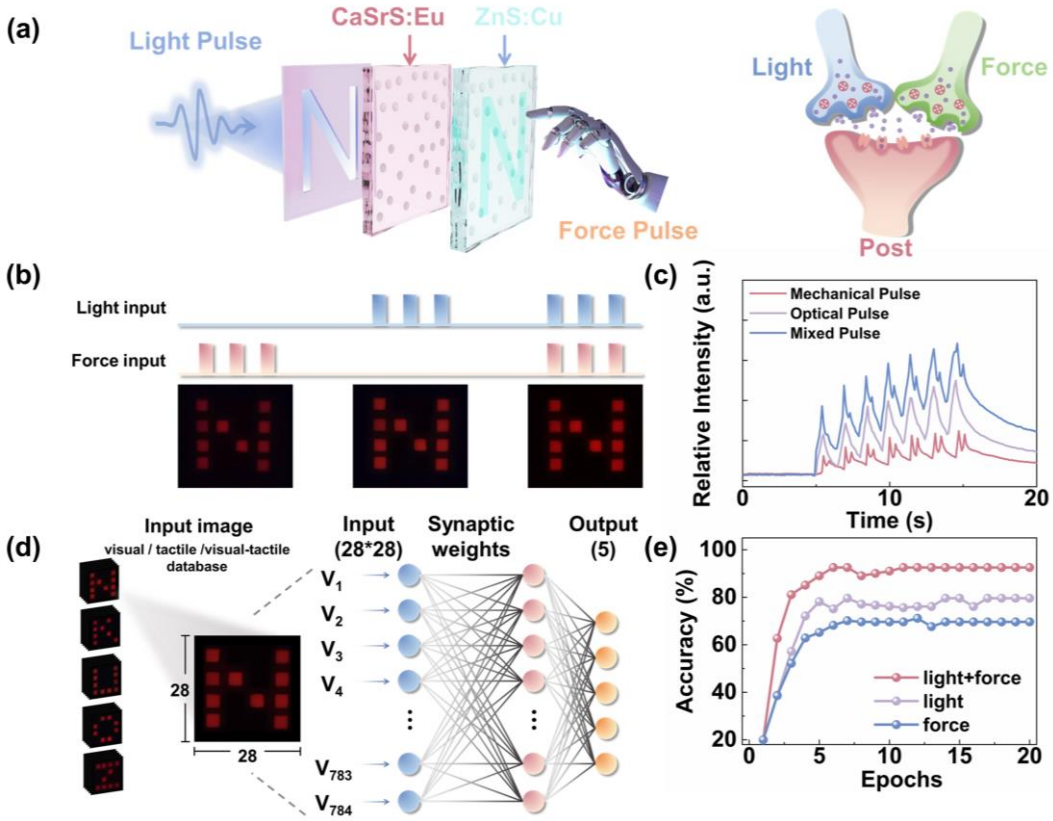

Figure 4. Enhanced image recognition achieved by visual-tactile perception array. a) Schematic of the device under synchronous force and light pulses with the schematic of the biological counterparts. b) The graphics of array device's responses after 30 mechanical, optical and synchronized optical-mechanical pulses. c) The response of the device to the individual or mixed inputs of light and force stimulus. d) Schematic of ANN architecture. e) The recognition accuracy of ANN variation with the training epoch number, under the force pulses, light pulses, or a combination of them.

The visual and tactile information including transparency, hardness offers important cues for human to recognize and identify materials. As depicted in **Figure 5**a, tactile receptors work to collect the hardness information of materials, and light signals are converted into electrical signal by retina and then sent to the visual cortex. Then, back-end neural networks will identify the materials based on both of the visual and tactile information. Inspired by this process, the artificial counterpart is designed and displayed in Figure 5b. Due to the difference between the tactile and visual perception responses of the synaptic device, the materials can be determined in a way similar to that of human sensing and processing system. Here, an ANN is constructed for categorizing the nine kinds of materials with distinguished hardness and transparency (Figure 5c). Subsequently, the different features of materials are represented by the device's response under force pulses of 12.5 kPa (1 s interval) and 2.5 mW cm^{-2} light pulses (pulse width of 0.5 s, 1 s interval, λ = 460 nm), respectively, and the responses of the device are detailed in **Figure S35** of Supporting Information. Taking transparent glass and PDMS as examples, Supplementary video 2 and video 3 demonstrate the PSL intensity data acquired from the device

under force pulses and light pulses, respectively, to reflect the transparency and hardness information of the materials. Before the identification, the details of flowchart to distinguish the light, force pulses and no-detection case are outlined in **Figure S36** of Supporting Information, which are considered as features to construct the samples in database. The database includes 450 samples which stand for various materials with diverse transparencies and hardnesses, and it was used to train the ANN with six input neurons (**Figure S37** of Supporting Information). The synaptic weights are displayed by the connections between the input, hidden and output layer, and the nine output neurons correspond to nine different materials (Figure 5d). As the training epochs increase, the identification accuracy increases. Additionally, increasing the pulse number enhances the contrast of visual and tactile information to make the identification accuracy higher (Figure 5e and **Figure S38** of Supporting Information). Notably, with seven force and light pulses, the confusion matrix between the predicted and target labels reveals an impressive accuracy of 98.6% (Figure 5f), showing the system's proficiency in identifying various materials. These findings demonstrate the potential of tactile-visual multimodal perception for accurate categorization, and may be adopted by future robots.

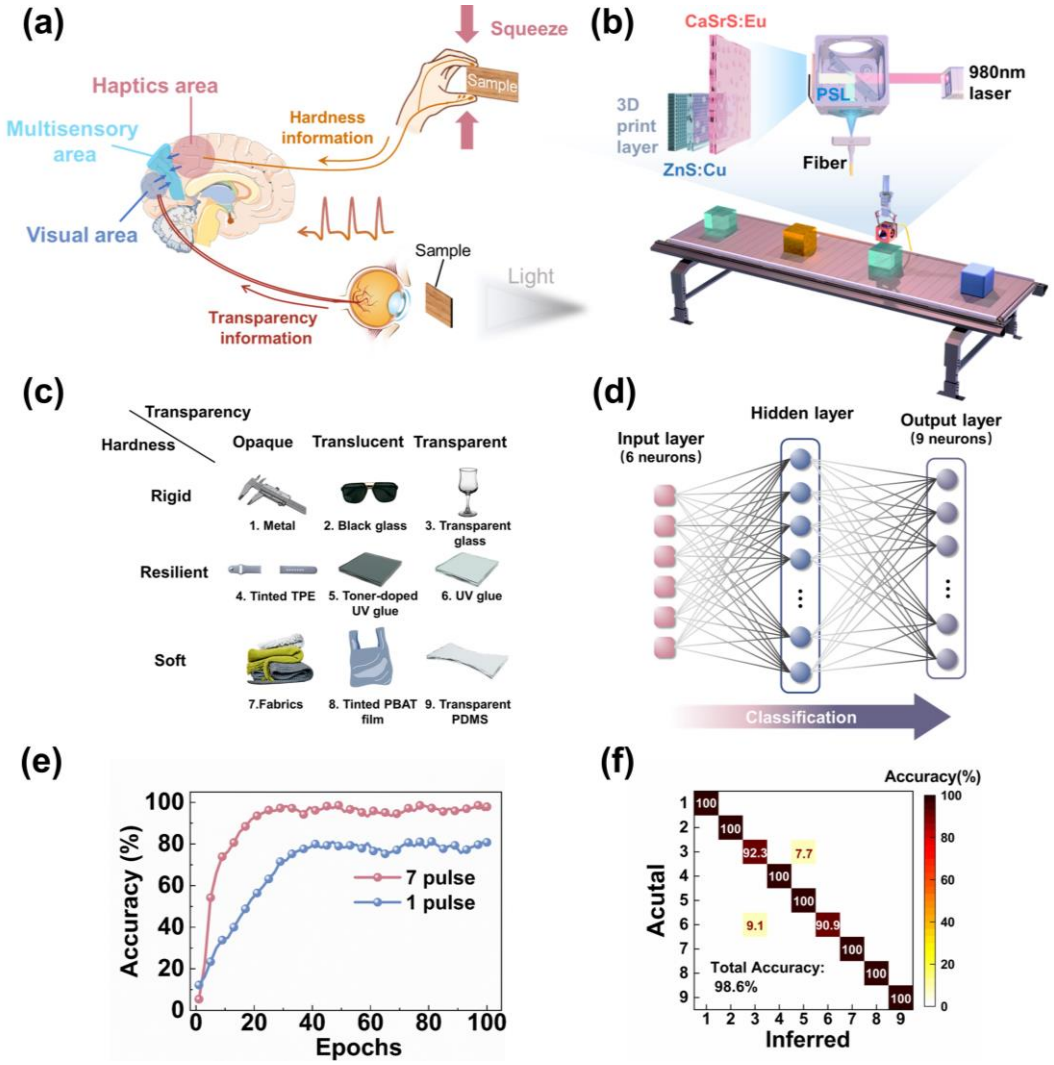

Figure 5. Material recognition achieved through the device's visual-tactile parallel response. a) Schematic diagram of the human brain using hardness and transparency information to implement material judgment. b) Schematic diagram of the in-sensor computing system for material recognition. c) Schematic of the nine materials selected, classified and numbered according to hardness and transparency. d) Schematic of ANN architecture. e) The identification accuracy of ANN variation with the training epoch number. The accuracy improves with the increase of number of pulses applied to the device. f) Confusion matrix showing the results of nine common materials identification.

3. Conclusion

In summary, inspired by biological nervous system's multimodal perception, we introduce an innovative visual-tactile fused artificial synapse which is capable of performing in-sensor computing in a remotely accessible manner. The mechano-optical perception, memory, and neuromorphic functions are integrated in the device; the synaptic behaviors such as adaptive plasticity are demonstrated. Besides, in-sensor computing can be implemented via optical states of PSL material to avoid redundant data movement, which will benefit large-scale integration

and data-intensive applications. Unlike visual-tactile sensors that rely on electrical signals to process the acquired information, the optical reading method employed in this work enables remote operation and offers easy accessibility. Additionally, the ML material ZnS:Cu demonstrates sensitive and self-reproducible mechano-optical conversion properties. As a result, pre- and post-irradiation are no longer essential, which alleviates numerous constraints in practical applications. Compared with the single sensing mode, the fusion of visual and tactile achieves a significant improvement in recognizing handwritten pattern from 69.6% to 92.5%. Furthermore, a high accuracy of 98.6% for identifying materials has been obtained based on the device. Our work illuminates a new strategy for designing multimodal perceptive neuromorphic devices using unique combinations of materials for future intelligent applications.

4. Methods

Phosphor Synthesis and Device Fabrication: ML phosphor ZnS:Cu was purchased from Global Tungsten & Powders Co.. PSL phosphor $Ca_{0.25}Sr_{0.75}S$:Eu (CaSrS:Eu) was prepared by the traditional high-temperature solid-state method. The raw materials CaS (99.99%), SrS (99.99%) and $EuCl_3 \cdot 6H_2O$ (99.9%) were purchased without further treatment. Stoichiometric ratio of raw materials was weighed, mixed and adequately ground for 30 min in an agate mortar. Then, the uniform mixture was transferred into alumina crucibles and sintered in a corundum tube furnace at 1000 °C for 4 h in a N_2 atmosphere. The ML phosphor composite was made by homogeneously mixing ZnS:Cu powders into the PDMS matrix at a weight ratio of 6:4. PDMS was made of base and crosslinker at a weight ratio of 10:1. The composite was placed in vacuum chamber for 30 mins to remove the air bubbles. Then the ZnS:Cu/PDMS composite was cured at 80 °C for 2 h followed by natural cooling. CaSrS:Eu phosphor was thoroughly mixed into the UV-curable adhesive (Norland NOA 61) matrix at a weight ratio of 3:7 and spin-coated on the ZnS:Cu/PDMS plate. Next, the sample was irradiated with UV lamp (365 nm) for 10 min for full curing. The mechanical microstructure layer was prepared using 3D-printing technology, with its surface having a spherical protrusion with a diameter of 0.5 mm.

Material Characterizations and Photoresponse Measurements: Scanning electron microscopy (SEM) and energy dispersive spectrometer (EDS) analysis were carried out by a Zeiss Sigma 500 field emission SEM system. XRD patterns were recorded by the Bruker D8 Advanced X-ray diffractometer with Cu Kα1 radiation (λ = 1.5406 Å). The x-ray photoelectron spectroscopy (XPS) measurements were performed by a ThermoFisher Scientific ESCALAB 250Xi instrument. ML and PSL spectra were measured using a PyLoN CCD camera coupled with SpectraPro 300i spectrophotometer. PSL spectra were measured using 980 nm LED lamp. The power was measured using laser power and energy meter (FieldMaxII-TOP, Coherent).

Luminescent decay curves were recorded with a photomultiplier (PMT, H11902-04, Hamamatsu) coupled with Tektronix DPO3034 oscilloscope. The luminescence photos were taken by a mirrorless camera (Sony NEX-5N) with a Sigma (56 mm 1.4) lens.

Artificial neural network construction: The input PSL signals x are multiplied by synaptic weights w (full connected layer), yielding learned features z that encapsulate light intensity signals. These light intensity signals are then passed through an activation function (sigmoid) to facilitate computations in the subsequent layers. To effectively optimize the synaptic weights w during the training process, the widely-used backpropagation (BP) algorithm has been employed. Typically, the gradient descent algorithm is used to update weights, as shown in Equations (1) and (2).

$$\Delta w = w' - w = -\eta \frac{\partial E}{\partial w} \quad (1)$$

$$E = L\ (t, y) \quad (2)$$

Herein, η represents the learning rate. t is the target output for a training sample. y is the actual output of the output neuron, and E is the loss function. The entire process is implemented in the Integrated Development Environment (IDE) in the Anaconda environment.

Supporting Information

Supporting Information is available from the Wiley Online Library or from the author.

Acknowledgments

This work was supported by the National Natural Science Foundation of China (No. 52233014, 12274243, 12074298, 52372160), the Research Grants Council of Hong Kong (PolyU SRFS2122-5S02), the Open Fund of State Key Laboratory of Information Photonics and Optical Communications (IPOC2022A02), the Fundamental Research Funds for the Central Universities, Shenzhen Science and Technology Program (Grant No. JCYJ2022053014061 4032), and “CUG Scholar” Scientifc Research Funds at China University of Geosciences (Wuhan) (Project No. 2022175).

Conflict of Interest

All authors declare no conflicts of interest.

Data Availability Statement

The authors declare that they have no competing interests.

Data and materials availability: All data supporting the results of this study are available in the manuscript or the supplementary information. Additional data are available from the corresponding author upon request.

Received: ((will be filled in by the editorial staff))
Revised: ((will be filled in by the editorial staff))
Published online: ((will be filled in by the editorial staff))

References

1. H. Jang, H. Hinton, W.-B. Jung, M.-H. Lee, C. Kim, M. Park, S.-K. Lee, S. Park, D. Ham, *Nat. Electron.* **2022**, 5, 519-525.
2. Y. Yang, C. Pan, Y. Li, X. Yangdong, P. Wang, Z.-A. Li, S. Wang, W. Yu, G. Liu, B. Cheng, Z. Di, S.-J. Liang, F. Miao, *Nat. Electron.* **2024**, 7, 225-233.
3. Z. Li, Z. Li, W. Tang, J. Yao, Z. Dou, J. Gong, Y. Li, B. Zhang, Y. Dong, J. Xia, L. Sun, P. Jiang, X. Cao, R. Yang, X. Miao, R. Yang, *Nat. Commun.* **2024**, 15, 7275.
4. D. Lee, M. Park, Y. Baek, B. Bae, J. Heo, K. Lee, *Nat. Commun.* **2022**,13, 5223.
5. J. Ko, D. Kim, Q.H. Nguyen, C. Lee, N. Kim, H. Lee, J. Eo, J.E. Kwon, S.-Y. Jeon, B.C. Jang, S.G. Im, Y. Joo, *Sci. Adv.* **2024**, 10, 0778.
6. X. Wu, S. Shi, B. Liang, Y. Dong, R. Yang, R. Ji, Z. Wang, W. Huang, *Sci. Adv.* **2024**, 10, 4524.
7. Y. Kim, A. Chortos, W. Xu, Y. Liu, J.Y. Oh, D. Son, J. Kang, A.M. Foudeh, C. Zhu, Y. Lee, S. Niu, J. Liu, R. Pfattner, Z. Bao, T.-W. Lee, *Science* **2018**, 360, 998-1003.
8. H. Li, J. Lin, S. Lin, H. Zhong, B. Jiang, X. Liu, W. Wu, W. Li, E. Iranmanesh, Z. Zhou, W. Li, K. Wang, *Nat. Commun.* **2024**, 15, 7632.
9. J. Lee, B.H. Jeong, E. Kamaraj, D. Kim, H. Kim, S. Park, H.J. Park, *Nat. Commun.* **2023**, 14, 5775.
10. K. Chen, H. Hu, I. Song, H.B. Gobeze, W.-J. Lee, A. Abtahi, K.S. Schanze, J. Mei, *Nat. Photonics* **2023**, 17, 629-637.
11. Y. Ni, J. Liu, H. Han, Q. Yu, L. Yang, Z. Xu, C. Jiang, L. Liu, W. Xu, *Nat. Commun.* **2024**, 15, 3454.

12. S.G. Sarwat, T. Moraitis, C.D. Wright, H. Bhaskaran, *Nat. Commun.* **2022**, 13, 2247.
13. Z. Chen, Z. Lin, J. Yang, C. Chen, D. Liu, L. Shan, Y. Hu, T. Guo, H. Chen, *Nat. Commun.* **2024**, 15, 1930.
14. T. Wang, J. Meng, X. Zhou, Y. Liu, Z. He, Q. Han, Q. Li, J. Yu, Z. Li, Y. Liu, H. Zhu, Q. Sun, D.W. Zhang, P. Chen, H. Peng, L. Chen, *Nat. Commun.* **2022**, 7, 7432.
15. C. Zhang, H. Dong, C. Zhang, Y. Fan, J. Yao, Y.S. Zhao, *Sci. Adv.* **2021**, 17, 3530.
16. H. Tan, Q. Tao, I. Pande, S. Majumdar, F. Liu, Y. Zhou, P.O.Å. Persson, J. Rosen, S. van Dijken, *Nat. Commun.* **2020**, 11, 1369.
17. J. Yu, X. Yang, G. Gao, Y. Xiong, Y. Wang, J. Han, Y. Chen, H. Zhang, Q. Sun, Z.L. Wang, *Sci. Adv.* **2021**, 7, 9117.
18. B. Hou, L. Yi, C. Li, H. Zhao, R. Zhang, B. Zhou, X. Liu, *Nat. Electron.* **2022**, 5, 682-693.
19. J. Pei, L. Deng, S. Song, M. Zhao, Y. Zhang, S. Wu, G. Wang, Z. Zou, Z. Wu, W. He, F. Chen, N. Deng, S. Wu, Y. Wang, Y. Wu, Z. Yang, C. Ma, G. Li, W. Han, H. Li, H. Wu, R. Zhao, Y. Xie, L. Shi, *Nature* **2019**, 572, 106-111.
20. W. Cao, H. Yu, X. Wu, S. Li, Q. Meng, C. Chen, *Technol Health Care* **2021**, 29, 609-614.
21. F.R. Willett, D.T. Avansino, L.R. Hochberg, J.M. Henderson, K.V. Shenoy, *Nature* **2021**, 593, 249-254.
22. Z. Zhou, K. Chen, X. Li, S. Zhang, Y. Wu, Y. Zhou, K. Meng, C. Sun, Q. He, W. Fan, E. Fan, Z. Lin, X. Tan, W. Deng, J. Yang, J. Chen, *Nat. Electron.* **2020**, 3, 571-578.
23. H. Lee, S.-H. Park, J.-H. Yoo, S.-H. Jung, J.-H. Huh, *Sensors* **2020**, 20, 785.
24. L. Gu, S. Poddar, Y. Lin, Z. Long, D. Zhang, Q. Zhang, L. Shu, X. Qiu, M. Kam, A. Javey, Z. Fan, *Nature* **2020**, 581, 278-282.
25. S. Sundaram, P. Kellnhofer, Y. Li, J.-Y. Zhu, A. Torralba, W. Matusik, *Nature* **2019**, 569, 698-702.
26. W.W. Lee, Y.J. Tan, H. Yao, S. Li, H.H. See, M. Hon, K.A. Ng, B. Xiong, J.S. Ho, B.C.K. Tee, *Sci. Robot.* **2019**, 4, 2198.
27. M. Romera, P. Talatchian, S. Tsunegi, F. Abreu Araujo, V. Cros, P. Bortolotti, J. Trastoy, K. Yakushiji, A. Fukushima, H. Kubota, S. Yuasa, M. Ernoult, D. Vodenicarevic, T. Hirtzlin, N. Locatelli, D. Querlioz, J. Grollier, *Nature* **2018**, 563, 230–234.
28. M.L. Rodríguez-Méndez, J.A. De Saja, R. González-Antón, C. García-Hernández, C. Medina-Plaza, C. García-Cabezón, F. Martín-Pedrosa, *Front. Bioeng. Biotechnol.* **2016**, 4, 81.
29. K. Wang, Y. Liao, W. Li, J. Li, H. Su, R. Chen, J.H. Park, Y. Zhang, X. Zhou, C. Wu, Z. Liu, T. Guo, T.W. Kim, *Nat. Commun.* **2024**, 15, 3505.

30. M.U.K. Sadaf, N.U. Sakib, A. Pannone, H. Ravichandran, S. Das, *Nat. Commun.* **2023**, 14, 5729.
31. H. Tan, Y. Zhou, Q. Tao, J. Rosen, S. van Dijken, *Nat. Commun.* **2021**, 12, 1120.
32. C. Jiang, J. Liu, Y. Ni, S. Qu, L. Liu, Y. Li, L. Yang, W. Xu, *Nat. Commun.* **2023**, 14, 1344.
33. X. Wu, E. Li, Y. Liu, W. Lin, R. Yu, G. Chen, Y. Hu, H. Chen, T. Guo, *Nano Energy* **2021**, 85, 106000.
34. C. Wan, P. Cai, X. Guo, M. Wang, N. Matsuhisa, L. Yang, Z. Lv, Y. Luo, X.J. Loh, X. Chen, *Nat. Commun.* **2020**, 11, 4602.
35. J. He, R. Wei, S. Ge, W. Wu, J. Guo, J. Tao, R. Wang, C. Wang, C. Pan, *InfoMat* **2024**, 6, 12493.
36. Q. Mao, Z. Liao, J. Yuan, R. Zhu, *Nat. Commun.* **2024**, 15, 6871.
37. S. Qu, L. Sun, S. Zhang, J. Liu, Y. Li, J. Liu, W. Xu, *Nat. Commun.* **2023**, 14, 7181.
38. X. Fan, I.M. White, *Nat. Photonics* **2011**, 5, 591-597.
39. Y. Li, Z. Guo, X. Zhao, S. Liu, Z. Chen, W.-F. Dong, S. Wang, Y.-L. Sun, X. Wu, *Nat. Commun.* **2024**, 15, 2906.
40. Z. Xie, Y. Xue, X. Zhang, J. Chen, Z. Lin, B. Liu, *Nat. Commun.* **2024**, 15, 3668.
41. W. Wang, S. Wang, Y. Gu, J. Zhou, J. Zhang, *Nat. Commun.* **2024**, 15, 2014.
42. C. Li, N. Schramma, Z. Wang, N.F. Qari, M. Jalaal, M.I. Latz, S. Cai, *Sci. Adv.* **2023**, 9, 8643.
43. K.-S. Sohn, S. Timilsina, S.P. Singh, T. Choi, J.S. Kim, *APL Mater.* **2016**, 4, 106102.
44. K S. Lin, H. Lin, C. Ma, Y. Cheng, S. Ye, F. Lin, R. Li, J. Xu, Y. Wang, *Light Sci. Appl.* **2020,** 9, 22.
45. F. Liu, W. Yan, Y.-J. Chuang, Z. Zhen, J. Xie, Z. Pan, *Sci. Rep.* **2013**, 3, 1554.
46. S. Hajra, S. Panda, S. Song, B. K. Panigrahi, P. Pakawanit, S. M. Jeong, H. J. Kim, *Nano Energy* **2023**, 114, 108668.
47. Y. Gao, R. Li, W. Zheng, X. Shang, J. Wei, M. Zhang, J. Xu, W. You, Z. Chen, X. Chen, *Chem. Sci.* **2019**, 10, 5452-5460.
48. D. Jia, J. Zhu, B. Wu, *J. Electrochem.* **2000**, 147, 3948.
49. L. Liang, J. Chen, K. Shao, X. Qin, Z. Pan, X. Liu, *Nat. Mater.* **2023**, 22, 289-304.
50. Y. Zhuang, D. Tu, C. Chen, L. Wang, H. Zhang, H. Xue, C. Yuan, G. Chen, C. Pan, L. Dai, R.-J. Xie, *Light Sci. Appl.* **2020**, 9, 182.
51. R.S. Zucker, W.G. Regehr, *Annu. Rev. Physiol.* **2002**, 64, 355-405.
52. S.L. Jackman, W.G. Regehr, *Neuron* **2017**, 94, 447-464.

Table of contents

A mechano-optical artificial synapse that enables in-sensor computing with visual-tactile perception is achieved by integrating photostimulated luminescence with self-recoverable mechanoluminescence materials. The multimodal artificial synapse demonstrates an individual and synergistic plasticity in a remotely accessible manner, and enables neuromorphic pattern recognition and materials identification. This work paves the way to construct flexible in-sensor computing systems with crossmodal integration and recognition.

Jiaxing Guo[┼], Feng Guo[┼], Huijun Zhao[┼], Hang Yang, Xiaona Du, Fei Fan, Weiwei Liu, Yang Zhang, [*] Dong Tu [*]& Jianhua Hao [*]

In-Sensor Computing with Visual-Tactile Perception Enabled by Mechano-Optical Artificial Synapse

ToC figure